Polyhedron 51 (2013) 243–254

Contents lists available at SciVerse ScienceDirect

Polyhedron

journal homepage: www.elsevier.com/locate/poly

New diethoxo-bridged dinuclear Cr(III) complexes with derivatives of the quinoxaline-2,3-dione ligand and 2,2′-bipyridine as a co-ligand: Syntheses, spectral characterizations, magnetic properties, antimicrobial inhibitory activities and interpretation of the electronic absorption spectra using the ZINDO/S-CI semi-empirical method

Attia S. Attia *, Ayman A. Abdel Aziz, Khalifa A. Alfallous, M.F. El-Shahat

Chemistry Department, Faculty of Science, Ain Shams University, Abbasia, Cairo 11566, Egypt

ARTICLE INFO

Article history:
Received 23 August 2012
Accepted 16 December 2012
Available online 11 January 2013

Keywords:
Quinoxaline
Chromium complex
Dimer
Bipyridine
Semi-empirical calculations
Antimicrobial activity

ABSTRACT

Two new diethoxo-bridged dinuclear Cr(III) complexes, $[Cr(QX)(bpy)EtO]_2$ [QX = 6,7-dichloroquinoxaline-2,3-dione (**1**); 6,7-dimethylquinoxaline-2,3-dione (**2**)], have been synthesized and characterized. The complexes were initially characterized on the basis of their elemental and mass analyses. The infrared studies were useful in assigning the coordination mode of the quinoxaline-2,3-dione ligand to the chromium metal. In addition, the presence of μ-ethoxo bridges was inferred from the characteristic vibrational bands in the IR spectra of both complexes. The structural and vibrational behaviors of both complexes have been elucidated using a parameterized PM3 semi-empirical method. The magnetic susceptibility, measured at 298 K, indicated exchange interactions between the two Cr(III) centers. The observed effective magnetic moments have been correlated to the calculated Cr···Cr distances and Cr–O–Cr angles of the $Cr(OEt)_2Cr$ cores in both complexes. The ESR spectra have been recorded on powder samples at 293 K. The dominant quintet state has been computer-simulated with the parameters $J = 23\ cm^{-1}$, $g = 2.11$, $D = 0.074\ cm^{-1}$ and $E = 0.008\ cm^{-1}$ for **1**. On the other hand, the spectrum of complex **2**, which showed two slightly different Cr centers, has been simulated with $J = 17\ cm^{-1}$, $g_1 = 2.17$, $D_1 = 0.063\ cm^{-1}$, $E_1 = 0.012\ cm^{-1}$ for site 1 and $g_2 = 2.055$, $D_2 = 0.065\ cm^{-1}$ and $E_2 = 0.0087\ cm^{-1}$ for site 2. The electronic spectra of the studied complexes were dominated by charge-transfer, [$Cr(d_\pi) \rightarrow bpy(\pi^*)$ and $QX(O\text{-}p_\pi) \rightarrow Cr(d_{\pi^*})$], and spin-allowed d–d transitions. In addition, low-energy maxima characteristics of the dinuclear transition metal complexes were observed in the 550–1050 nm region. Theoretical studies of the electronic spectra by the ZINDO/S-CI method were useful in interpreting the observed electronic transitions. The antimicrobial activity studies have indicated a significant inhibitory activity of complex **2** against the studied bacteria and complex **1** showed the highest inhibitory activity against the studied fungi.

1. Introduction

Understanding the influence of intermolecular interactions on the magnetic and spectroscopic properties of multinuclear transition metal centers has been long-standing interest in inorganic chemistry, especially due to the presence of metal clusters in biological systems [1]. Metalloproteins containing multinuclear active sites exhibit unique ground state properties and excited state spectral features which are associated with the interactions between the metal centers. The excited states of binuclear transition metal systems have also been known to exhibit spectroscopic effects due to dimer interactions [2]. Thus, intensity enhancements of the low-energy bands corresponding to ligand-field d–d transitions have been observed for dinuclear Cr(III), Mn(II) and Fe(III) complexes as a result of the dinuclear interactions [3–5].

Due to the dependence of the dinuclear interactions on both the structure and symmetry of the organic ligands coordinating to the central metals in the complexes, dinuclear μ-OR species bearing various chelating ligands offer interesting possibilities to tune the metal-to-metal exchange interactions by small structural changes of the peripheral ligands and the μ-OR moieties [6]. With respect to the μ-OR unit, the magnetic exchange interaction between the metal centers in dimeric complexes has been shown to vary with the M–O–M bridging angle and the M–O bond length [7].

* Corresponding author. Tel.: +20 2 6717 839.
E-mail address: attiasattia@hotmail.com (A.S. Attia).

0277-5387/$ - see front matter © 2013 Elsevier Ltd. All rights reserved.
http://dx.doi.org/10.1016/j.poly.2012.12.034

Our interest in this field has been focused on μ-oxo, μ-hydroxo and μ-methoxo dinuclear Fe, Cr and Mo complexes [8–11]. In the present work, we have developed a synthetic procedure to synthesize two new di-μ-ethoxo dinuclear Cr(III) complexes with the general chemical formulae $[Cr(DCQX)(bpy)EtO]_2$ and $[Cr(DMQX)(bpy)EtO]_2$ (DCQX = 6,7-dichloroquinoxaline-2,3-dione; DMQX = 6,7-dimethyquinoxaline-2,3-dione). To the best of our knowledge, these dimeric complexes are considered to be amongst the few di-μ-ethoxo binuclear dichromium(III) complexes that have been reported and are the first di-μ-ethoxo binuclear dichromium(III) complexes of the quinoxaline-2,3-dione ligand. Our aim is to synthesize two dimeric complexes of the quinoxaline-2,3-dione ligand and to study the effects of structural changes in the ligand on the magnetic, spectroscopic and biological behaviors of the complexes.

2. Experimental

Chromium hexacarbonyl ($Cr(CO)_6$), 2,2′-bipyridine (bpy), oxalic acid ($C_2H_2O_4{\cdot}2H_2O$), 4,5-dichloro-1,2-phenylenediamine and 4,5-methyl-1,2-phenylenediamine were used as purchased from Sigma–Aldrich Chemical Co. Inc. The 6,7-dichloroquinoxaline-2,3-dione (DCQX) and 6,7-dimethylquinoxaline-2,3-dione (DMQX) ligands were synthesized following the reported procedure [12]. All solvents were dried according to standard procedures.

Elemental analysis was performed using a Perkin–Elmer 2400 CHN elemental analyzer. The mass spectra were obtained on a JEOL JMS-AX500 mass spectrometer. The infrared spectra (4000–400 cm^{-1}) were recorded as KBr pellets on a Unicam Mattson 1000 FTIR spectrometer. Magnetic susceptibility measurements were carried out on a Sherwood MK1 Scientific Magnetic Susceptibility Balance at 298 K. The EPR spectra were recorded on powder samples at the X-band (9.75 GHz) with an EMX Bruker spectrometer at 293 K. The electronic absorption spectra were recorded using a Unicam UV2-300 UV–Vis spectrometer. The sample concentrations of 5.08×10^{-4} and 5.14×10^{-4} mol dm^{-3} for $[Cr(DCQX)(bpy)EtO]_2$ and $[Cr(DMQX)(bpy)EtO]_2$, respectively, in DMSO were measured against the solvent in the reference cell.

The antimicrobial activity of tested samples of the ligands and the complexes were determined using a modified Kirby–Bauer disc diffusion method [13]. A 100 μL of the tested bacteria or fungi were grown in 10 mL of fresh media until they reached a count of approximately 108 cells/mL for bacteria and approximately 105 cells/mL for fungi. A 100 μL of microbial suspension was spread onto agar plates corresponding to the broth in which they were maintained. Plates inoculated with Gram-positive bacteria (*Staphylococcus aureus*) and Gram-negative bacteria (*Escherichia coli*) were incubated at 35–37 °C for 24–48 h whereas, filamentous fungus (*Aspergillus flavus*) and yeast fungus (*Candida albicans*) were incubated at 25 °C for 48 h and 30 °C for 24–48 h, respectively. Then the diameters of the inhibition zones were measured in millimeters. Standard discs of tetracycline (antibacterial agent) and Amphotericin (antifungal agent) served as positive controls for the antimicrobial activity, while filter discs impregnated with 10 μL of DMSO solvent were used as a negative control. Blank paper discs with a diameter of 8.0 mm were impregnated with 10 μL of the tested samples stock solution (0.02 g/ mL) and inhibition zone diameters were measured.

The semi-empirical calculations in this study have been carried out using the HYPERCHEM 7.5 program package [14]. The Polak–Ribiere version of the conjugate gradient method was used in all energy minimization calculations with a coverage criterion less than 1.0×10^{-3} kcal mol^{-1} $Å^{-1}$. First and separately the DCQX and DMQX ligands have been optimized and the results obtained have been applied in each calculation thereafter. The values of Cr–O and Cr–N bond lengths and angles in the literatures were used as the starting inputs [15–19]. Initial optimization of the complexes was performed by molecular mechanics (MM+). The geometry was further refined using the parameterized PM3 method. Available parameters for Cr and Cl elements were implemented in the PM3 semi-empirical method [20,21], then the parameterized PM3 method was used for geometry optimization of the complexes under study. Triplet state URHF spin pairing has been selected in addition to the standard SCF (with accelerated convergence). The theoretical harmonic vibrational frequencies were related to the experimental fundamentals by the optimum scaling factor λ, determined through a least-squares procedure given by $\lambda = \sum_i^{all} \omega_i^{theor} \nu_i^{exp\,t} / \sum_i^{all} (\omega_i^{theor})^2$, where ω_i^{theor} and $\nu_i^{exp\,t}$ are the ith theoretical harmonic and ith experimental fundamental frequencies (in cm^{-1}) [22]. The molecular root mean square error (rms) was calculated by the square root of the sum over all the modes of Δ_{min} given in Ref. [22], where Δ_{min} is the minimized residual for each mode. The ZINDO/S-CI method is parameterized to produce UV–Vis electronic transitions and has been used to estimate the energies and shapes of the frontier orbitals for the complexes [23,24]. The maximum excitation energy for configuration interaction calculations was 8.0 eV. The overlap weighing factors $f_{\sigma\sigma}$ and $f_{\pi\pi}$ were taken as 1.267 and 0.585, which had been used with good success for transition metals [25,26].

EasySpin, a computational package for spectral simulation and analysis in ESR based on Matlab computational software, was used to perform a simulation of the experimental ESR spectra of the two dimeric complexes [27].

2.1. Synthesis of the $[Cr(DCQX)(bpy)EtO]_2$ complex (**1**)

2,2′-Bipyridine (0.071 g, 0.455 mmol) was added to a solution containing 0.100 g (0.454 mmol) of $Cr(CO)_6$ in 50 mL of THF. The mixture was refluxed for 2 h with continuous stirring. The resulting orange colored solution was cooled down to room temperature. DCQX (0.104 g, 0.450 mmol) was dissolved in 20 mL of EtOH and slowly added to the reaction mixture. The contents were refluxed for 18 h with continuous stirring, and during this time the brown solid product separated from solution. The solid was isolated, washed with 15 mL THF/EtOH (1:1) and dried in vacuum. A concentrated solution of the product in DMSO/EtOH (3:1) was allowed to evaporate slowly for 2 weeks, which resulted in a reddish-brown powder. Washing the powdery solid with EtOH followed by diethyl ether and then drying overnight in vacuum resulted in 0.13 g (59.6% yield) of the pure product (one brown spot in a TLC test). Attempts to obtain crystals suitable for X-ray crystallography were unsuccessful due to the limited solubility of the synthesized complex in most common solvents.

Anal. Calc. for $C_{40}H_{34}Cl_4Cr_2N_8O_6$ (Mr = 968.55): C, 49.60; H, 3.54; Cl, 14.64; N, 11.57. Found: C, 49.53; H, 3.52; Cl, 14.70; N, 11.62%. Effective magnetic moment at 298 K, μ_{eff} (BM): 2.955.

2.2. Synthesis of the $[Cr(DMQX)(bpy)EtO]_2$ complex (**2**)

The $[Cr(DMQX)(bpy)EtO]_2$ complex was synthesized with a similar procedure to that for $[Cr(DCQX)(bpy)EtO]_2$ using DMQX (0.086 g, 0.452 mmol) instead of DCQX. A brown powder of the product was obtained (0.11 g, 54.9% yield) after recrystallization of a concentrated solution of the complex from DMSO/EtOH/benzene (4:1:0.3).

Anal. Calc. for $C_{44}H_{46}Cr_2N_8O_6$ (Mr = 886.89): C, 59.58; H, 5.23; N, 12.64. Found: C, 59.48; H, 5.25; N, 12.67%. Effective magnetic moment at 298 K, μ_{eff} (BM): 3.116.

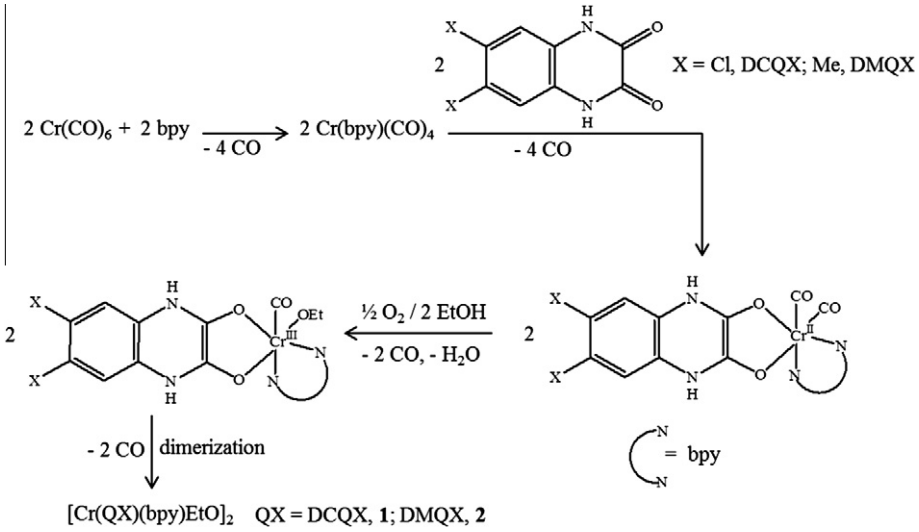

Scheme 1. Suggested mechanism for the formation of the dinuclear Cr(III) complexes **1** and **2**.

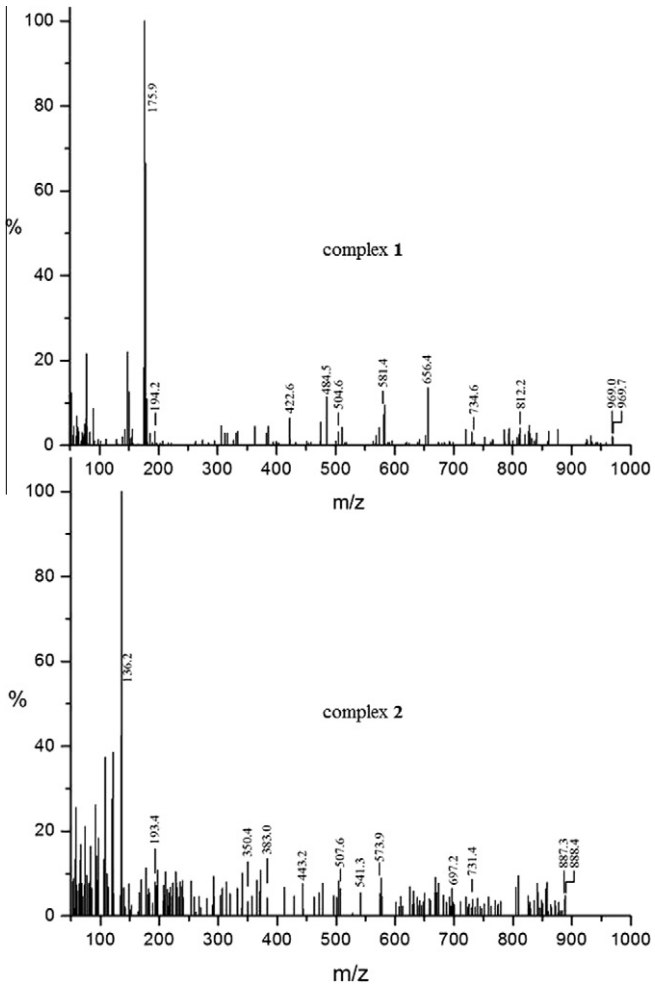

Fig. 1. The mass spectra for the dichromium complexes **1** and **2**.

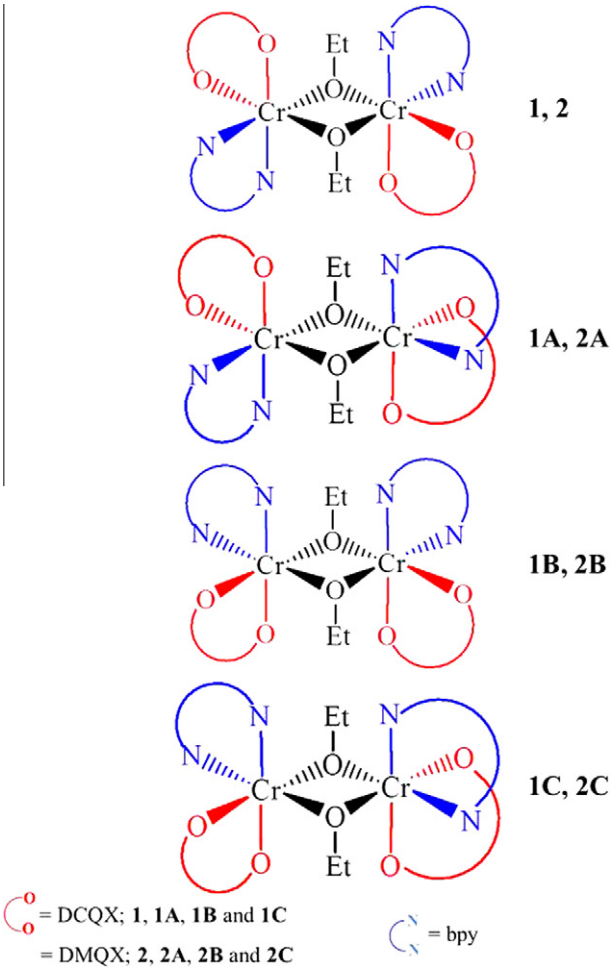

Fig. 2. Chemical structures of complexes **1** and **2** used for the semi-empirical calculations.

3. Results and discussion

The stoichiometric reactions between $Cr(CO)_6$ and 2,2′-bipyridine in THF solvent followed by addition of 6,7-dichloroquinoxaline-2,3-dione (DCQX) or 6,7-dimethylquinoxaline-2,3-dione (DMQX) in EtOH under atmospheric pressure have yielded two dinuclear Cr(III) complexes with the chemical formulae $[Cr(DCQX)(bpy)EtO]_2$ (**1**) and $[Cr(DMQX)(bpy)EtO]_2$ (**2**). It was

Table 1
Calculated results for the structures of complex **1** (**1**, **1A**, **1B** and **1C**) and complex **2** (**2**, **2A**, **2B** and **2C**) obtained from parameterized PM3 semi-empirical calculations.

Calculated results (kcal/mol)	1	1A	1B	1C	2	2A	2B	2C
Total energy	−232814.05	−232751.22	−232765.13	−232787.52	−218797.03	−218770.30	−218768.95	−218793.31
Heat of formation	−327.11	−264.27	−278.19	−300.58	−340.04	−287.33	−286.02	−310.38

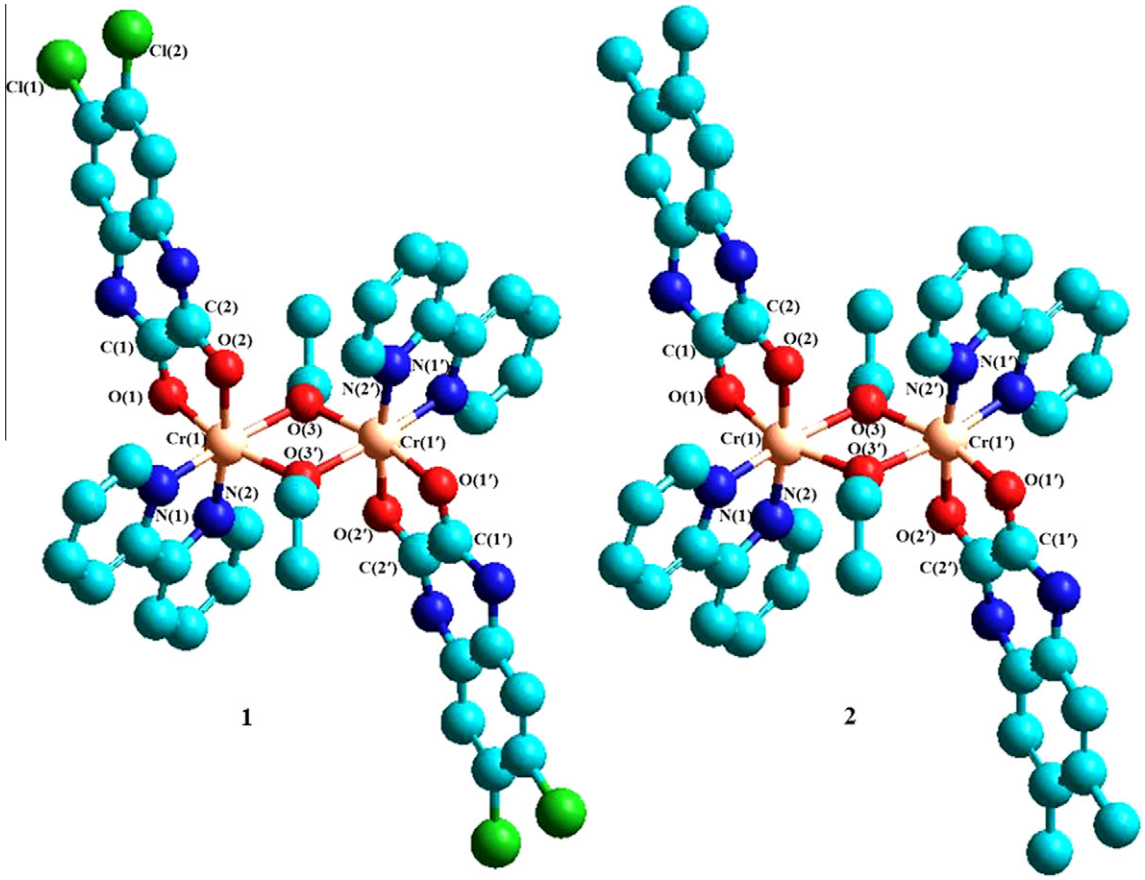

Fig. 3. The most stable geometries for complexes **1** and **2** based on the semi-empirical PM3 geometry optimization. Hydrogen atoms are omitted for clarity.

suggested that these dimeric complexes might be formed as a result of a two-electron oxidative-addition reaction of quinoxaline-2,3-dione (QX) to Cr(0) with the reduction of the former to quinoxaline-ene-2,3-diolate and the formation of the $[Cr^{II}(QX)(bpy)(CO)_2]$ intermediate. This behavior is similar to the two-electron oxidative-addition reactions of *o*-quinones to transition metal carbonyls, which result in reduction of the two C=O groups and the formation of a C=C bond between the two C–O groups formed [28–30]. This is followed by oxidation of the $[Cr^{II}(QX)(bpy)(CO)_2]$ intermediate complex by atmospheric oxygen to give the monomeric $[Cr^{III}(QX)(bpy)(CO)EtO]$ complex. Finally, two molecules of the later complex dimerise through two ethoxo groups, forming di-μ-ethoxo bridges between the Cr(III) centers (Scheme 1). The complexes were initially characterized based on their elemental analyses and mass spectra.

The mass spectra shown in Fig. 1 were very useful in assigning the composition of the two dimeric complexes. The mass spectra of complex **1** exhibited parent peaks due to the molecular ions $[M]^+$ and $[M+1]^+$ at (*m/z*) values of 969.0 and 969.7, respectively. For complex **2** similar peaks were observed at 887.3 and 888.4. Fragments corresponding to the molecular ions $[M-bpy]^+$, $[M-2bpy]^+$, $[M-DCQX]^+$, $[M-2DCQX]^+$ and $[M-(bpy+DCQX)]^+$ were observed for complex **1** at (*m/z*) values of 812.2, 656.4, 734.6, 504.6 and 581.4, respectively. Analogous peaks for the $[Cr(DMQX)(bpy)EtO]_2$ complex (**2**) were observed at (*m/z*) values of 731.4, 573.9, 697.2, 507.6 and 541.3. Fragments corresponding to half the molecular weight of the complex were observed in the mass spectra at *m/z* values of 484.5 for complex **1** and 443.2 for complex **2**. Other fragments that can be attributed to $[Cr(OEt)_2Cr]$ unit were observed for complexes **1** and **2** at 194.2 and 193.4, respectively. These results suggest dinuclear chromium complexes with the two Cr centers connected together by di-μ-ethoxo groups and each Cr metal bonded to QX and a bpy ligand.

The infrared studies of the synthesized complexes were useful in assigning the coordination mode of the QX ligand to the chromium metal centers. The infrared spectra of the free QX ligands displayed characteristic vibrational bands due to the stretching frequencies of N–H, C–H (aromatic) and C=O groups. These bands were observed for the DCQX ligand at 3416 and 3332 cm^{-1} (N–H), 3062 and 3043 cm^{-1} (C–H) and 1726 cm^{-1} (C=O), whereas for the DMQX ligand these bands were observed at 3437 and 3325 cm^{-1}, 3071 and 3050 cm^{-1}, and 1721 cm^{-1}. Additional vibrational frequencies corresponding to C–H stretches of the methyl groups were observed for the DMQX ligand at 2948 and 2867 cm^{-1}. The main characteristic feature of the IR spectra of the two dinuclear complexes was the slight shift of the stretching

Table 2
Selected bond lengths (Å) and angles (°) for complexes **1** and **2** obtained from the parameterized PM3 geometry optimization.

	Complex **1**	Complex **2**
Bond lengths		
Cr(1)–O(1)	1.939	1.934
Cr(1)–O(2)	1.974	1.973
Cr(1)–N(1)	1.984	1.979
Cr(1)–N(2)	1.985	1.982
Cr(1)–O(3)	1.997	1.999
Cr-(1)–(O3′)	1.971	1.962
C(1)–O(1)	1.338	1.340
C(2)–O(2)	1.323	1.323
Cr(1′)–O(1′)	1.939	1.930
Cr(1′)–O(2′)	1.974	1.944
Cr(1′)–N(1′)	1.984	1.960
Cr(1′)–N(2′)	1.985	1.975
Cr(1′)–O(3)	1.971	1.961
Cr(1′)–O(3′)	1.996	1.980
C(1′)–O(1′)	1.337	1.340
C(2′)–O(2′)	1.323	1.326
Cr(1)···Cr(1′)[a]	3.064	3.112
Bond angles		
O(1)–Cr(1)–O(2)	85.1	85.2
N(1)–Cr(1)–N(2)	81.6	81.7
O(1)–Cr(1)–O(3′)	164.2	161.8
N(1)–Cr(1)–O(3)	168.2	167.2
O(2)–Cr(1)–N(2)	171.9	172.4
O(1′)–Cr(1′)–O(2′)	85.1	84.6
N(1′)–Cr(1′)–N(2′)	81.6	80.8
O(1′)–Cr(1′)–O(3)	164.8	162.4
N(1′)–Cr(1′)–O(3′)	167.9	167.1
O(2′)–Cr(1′)–N(2′)	172.0	173.5
Cr(1)–O(3)–Cr(1′)	100.7	103.4
Cr(1)–O(3′)–Cr(1′)	100.8	104.3
O(3)–Cr(1)–O(3′)	79.2	75.9
O(3)–Cr(1′)–O(3′)	79.3	76.2
Cr(1)–O(3)–Cr(1′)–O(3′)[b]	0.74	2.54

[a] Distance between Cr(1) and Cr(1′).
[b] Torsion angle of the $Cr(O_2)Cr$ unit.

vibrations corresponding to N–H groups, which may indicate that the lone pair of electrons on the nitrogen do not contribute to the coordination of the DCQX or DMQX ligand with the Cr(III) center in their complexes [31]. In contrast, the bands that correspond to C=O stretches disappeared and two new bands, corresponding to C–O (coordinated) and C=C, were observed at ~1246 and ~1631 cm^{-1} for both complexes. The observed values for the C–O stretches are in good agreement with those reported for *o*-catecholates coordinated to transition metal ions [32–34]. Another important feature of the IR spectra of both complexes was three bands characteristic of μ-ethoxo ligands and these were observed at 1099, 1068 and 888 cm^{-1} for complex **1** and at 1106, 1062 and 890 cm^{-1} for complex **2**. Wu et al. [35] have reported that ethoxo-bridged dimers show three bands, characteristic of the ethoxo group, located in the IR spectrum near 1100, 1050 and 890 cm^{-1}. Characteristic absorptions of the coordinated bpy ligand, due to the out-of-plane deformation mode of the two equivalent sets of four hydrogen atoms on the rings, were observed at 806 and 770 cm^{-1} for complex **1** and at 805 and 774 cm^{-1} for complex **2** [36–39]. Finally, additional vibrations corresponding to C–H stretches of the methyl groups were observed in the spectrum of complex **2**.

The results obtained from the spectroscopic techniques are in good agreements with the suggested formula for the two dimeric complexes, but unfortunately they give no information about their geometries. Each of the dimeric complexes was expected to adopt one of the geometrical isomers shown in Fig. 2; **1**, **1A**, **1B** or **1C** (for complex **1**) and **2**, **2A**, **2B** or **2C** (for complex **2**), since experimentally only one product was isolated for each complex. Therefore, it is considered worthwhile to model the complexes using molecular mechanics MM+ and PM3 calculations, especially with the lack of structural analysis due to the difficulty in obtaining suitable crystals of the synthesized complexes.

The semi-empirical PM3 calculated results for each structure are summarized in Table 1. It can be seen that the geometrical structures (**1**, **1C**, **2** and **2C**) in which the two equatorial N-atoms (or the two equatorial O-atoms) are in *trans*-positions to one another have lower energies. The geometrical structures **1** and **2**, in which the similar ligands are in *trans*-positions to one another, are more stable than isomers **1C** and **2C** by 26.53 and 29.66 kcal/mol, respectively. The most stable structures **1** and **2** for the two dimeric complexes, based on the semi-empirical PM3 geometry optimization, are shown in Fig. 3. Selected bond lengths and angles are given in Table 2. The structures of the two dimeric complexes consist of two (QX)(bpy)Cr(III) units bridged by di-μ-ethoxo groups. In each (QX)(bpy)Cr(III) unit, the Cr(III) ion is coordinated to a quinoxaline-2,3-dione (QX) ligand through the reduced C–O groups and a bpy ligand. Each Cr(III) ion adopts a distorted octahedral geometry as the angles around the metal center deviates significantly from 90°, with the largest deviations being for the O(3)–Cr(1)–O(3′) angle (Table 2). Such geometrical features have been observed for several di-μ-hydroxo and di-μ-alkoxo dinuclear Cr(III) complexes [6,18,40,41]. While the dimeric complexes exhibited similar structural features, the distortion around each Cr(III) ion in complex **2** is non-symmetrical. In addition, the bridging Cr–O–Cr angles in complex **1** were 100.7° and 100.8°, whereas the corresponding angles in complex **2** were 103.4° and 104.3°. These resulted in Cr···Cr separations of 3.064 and 3.112 Å for complexes **1** and **2**, respectively. The Cr–O–Cr bridging angle and Cr···Cr separation reported for $[Cr(HL)_2(\mu\text{-}OCH_3)]_2$ (H_2L = 2-salicyloylhydrazono-1,3-dithiolane) were 100.9° and 3.02 Å, whereas those reported for $[Cr(3\text{-}Br\text{-}acac)_2(\mu\text{-}OEt)]_2$ (3-Br-acac = 3-bromo-2,4-pentanedionato) were 101.8° and 3.027 Å [6,15]. Although the calculated values for complex **2** were larger, they are still within the range reported for some dinuclear Cr(III) complexes [16,18,40,41]. These differences in the bridging angles and Cr···Cr separations for both **1** and **2** might explain the discrepancies in their magnetic and ESR behaviors (*vide infra*). The average Cr–O(QX) bond lengths for both complexes are in the range 1.934–1.957 Å, with the axial Cr–O bond being slightly longer. They are comparable to the average Cr–O values of 1.935 and 1.947 Å reported for $[(t\text{-butyl-acacen})CrOH]_2$ and $[(salen)CrOH]_2$, respectively [40]. In contrast, the average Cr–N(bpy) bond lengths for both complexes were shorter by about 0.07 Å than those reported for $[Cr(phen)_2OH]_2$ and $[Cr(bpy)(OH_2)Cl_3]$ complexes [18,19]. Finally, the average C–O values of 1.33 Å for both complexes are in good agreement with those reported for $[Cr(Cat)_3]^{3-}$ [17].

The observed and calculated vibrational frequencies for configurations **1** and **2** are compared in Table 3. The optimized scale factors determined for **1** and **2** were 0.9995696 and 1.0008961, respectively. The calculated harmonic vibrational frequencies compare well with the fundamental experimental frequencies. The calculated root mean square error (rms) per molecule was 21.56 and 36.74 cm^{-1} for **1** and **2**, respectively. These rms values compare very well with those reported for the vibrational frequencies calculations using HF/6-31G(d,p), MP2-fc/631G(d,p) and B-LYP/6-31G(d) [22].

Magnetic susceptibility measurements for the synthesized complexes have been recorded on solid samples at 298 K and have revealed effective magnetic moments of 2.955 and 3.116 BM for complexes **1** and **2**, respectively. These values are considerably lower than the theoretical value expected for two uncoupled Cr(III) centers with $S = 3/2$ (5.477 BM, assuming $g = 2.0$). Such behavior was reported for several di-μ-hydroxo and di-μ-alkoxodinuclear Cr(III) complexes, in which the unpaired electrons of the two Cr(III)

Table 3
Characteristic calculated and observed vibrational frequencies (cm^{-1}) for the dinuclear chromium (III) complexes **1** and **2**.

Vibrational frequencies (cm^{-1})[a,b]				Assignment[c]
Complex **1**		Complex **2**		
Calcd	Obsd	Calcd	Obsd	
3411.1	3417.1(s,b)	3428.3	3429.2(s,b)	ν_{asymm}N–H
3356.4	3356.2(s,b)	3345.1	3344.8(sh)	ν_{symm}N–H
3117.8	3109.2(m)	3111.4	3116.4(w)	νC–H aromatic rings (QX + bpy)
3061.0	3058.7(sh)	3087.4	3094.2(m)	νC–H aromatic rings (QX + bpy)
3041.4	3043.3(sh)	3057.1	3054.3(sh)	νC–H aromatic rings (QX + bpy)
		3026.6	3025.4(sh)	νC–H aromatic rings (QX + bpy)
2979.3	2984.6(sh)	2975.1	2971.0(sh)	νC–H (EtO)
2917.7	2922.2(m,b)	2925.6	2926.1(s,b)	νC–H (EtO)
2887.3	2876.9(sh)	2896.2	2898.6(sh)	νC–H (EtO)
		2867.3	2865.9(m,b)	νC–H (QX-CH_3)
		2855.2	2856.6(sh)	νC–H (QX-CH_3)
1628.0	1630.6(sh)	1635.7	1631.3(sh)	νC=C heterocyclic ring
1606.4	1607.7(sh)	1608.1	1606.5(vs)	νC=N (bpy)
1585.9	1586.0(vs)	1572.4	1586.0(sh)	νC=C aromatic + ring
1469.4	1490.9(s)	1496.3	1497.4(m)	Deformation (QX + bpy)
1443.9	1446.3(m)	1477.8	1469.6(sh)	Ring deformation (QX + bpy) + γCH_2 (EtO)
		1439.2	1446.3(s)	
1375.2	1379.3(s)	1401.9	1381.0(vs)	Ring deformation (QX + bpy) + γCH_3 (EtO)
1250.1	1246.3(s)	1253.3	1245.8(s)	νC–O (QX)
1163.2	1163.3(w)	1172.7	1162.2(m)	δCC + δC–H (bpy)
1134.9	1132.3(sh)	1132.1	1132.4(sh)	δCC + δC–H (bpy)
1038.0	1034.1(m)	1032.0	1030.1(m)	δCC + δC–H (bpy)
1097.2	1098.7(w)	1105.8	1105.6(w)	ν_{asymm}C–O (EtO)
1061.8	1067.8(s)	1071.0	1062.4(s)	ν_{symm}C–O (EtO)
889.7	887.8(s)	890.3	889.5(m)	δC–O (EtO)
802.8	806.3(s)	809.3	804.8(s)	γC–H (bpy)
768.0	769.5(s)	775.6	774.0(s)	γC–H (bpy)
734.7	734.8(m)	728.6	732.9(m)	ν_{asymm}O(QX)–Cr–O(EtO)
727.2	729.2(s)	661.5	662.5(w)	ν_{asymm}O(QX)–Cr–N(bpy)
548.6	549.1(s)	547.5	548.2(s)	νCr–O(EtO)
515.4	515.4(sh)	481.2	479.9(w)	νCr–O(QX)
455.6	455.5(w)	458.0	460.1(w)	νCr–N(bpy)

[a] w, weak; m, medium; s, strong; vs, very strong; b, broad.
[b] The calculated root mean square error (rms/molecule): 21.56 cm^{-1} (complex **1**); 36.74 cm^{-1} (complex **2**).
[c] QX, DCQX or DMQX; bpy, 2,2′-bipyridine; EtO, ethoxo bridging ligand.

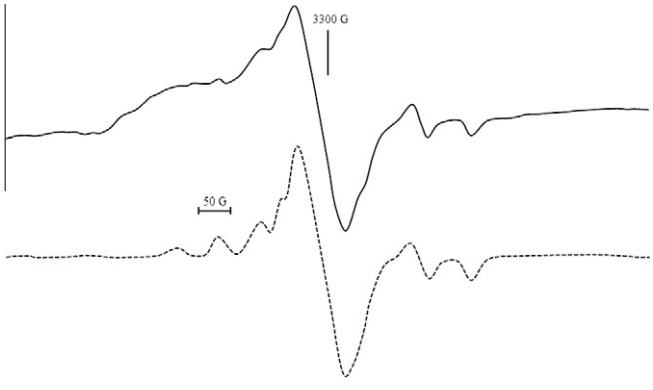

Fig. 4. X-band EPR spectra of complex **1**. Solid curve: experimental spectrum measured on a powder sample at 293 K. Dotted curve: simulated spectrum with $J = 23\ cm^{-1}$, $g = 2.11$, $D = 0.074\ cm^{-1}$ and $E = 0.008\ cm^{-1}$.

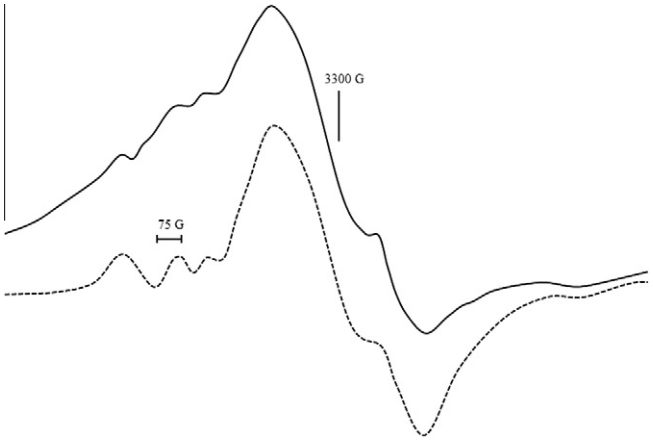

Fig. 5. X-band EPR spectra of complex **2**. Solid curve: experimental spectrum measured on a powder sample at 293 K. Dotted curve: simulated spectrum with the parameters $J = 17\ cm^{-1}$, $g_1 = 2.17$, $D_1 = 0.063\ cm^{-1}$, $E_1 = 0.012\ cm^{-1}$ cm^{-1} for site 1 and $g_2 = 2.055$, $D_2 = 0.065\ cm^{-1}$ and $E_2 = 0.0087\ cm^{-1}$ for site 2.

ions are antiferromagnetically coupled through the bridging groups [6,16,41,42]. The magnitude of the antiferromagnetic exchange interactions between the two Cr(III) centers through the bridged groups was found to be dependent on the Cr···Cr distance and the Cr–O–Cr angle of the $Cr(OR)_2Cr$ core [7,43]. This might explain the difference between the magnetic moments of both complexes, with a stronger exchange interaction for complex **1**. These results agree with the Cr···Cr distances and Cr–O–Cr angles obtained for both complexes from the semi-empirical calculations (Table 2).

The X-band EPR spectra recorded at 293 K on powder samples of the two dimeric complexes are shown in Figs. 4 and 5. The EPR spectra of complexes, containing two Cr(III) ions ($S = 3/2$), are expected to display resonances due to spin states $S = 1$–3. The resonances due to triplet ($S = 1$) and septet ($S = 3$) spin states are difficult to observe in the X-band EPR because the zfs in these

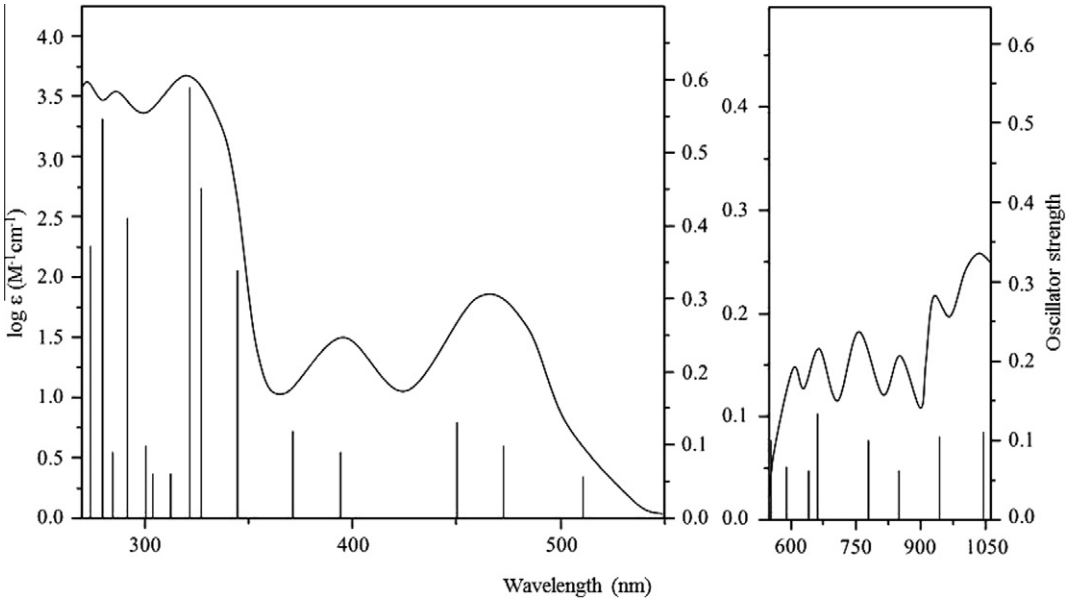

Fig. 6. The observed electronic spectrum in DMSO (curve) and the computed transitions resulting from ZINDO/S-CI calculations (lines) of complex **1**.

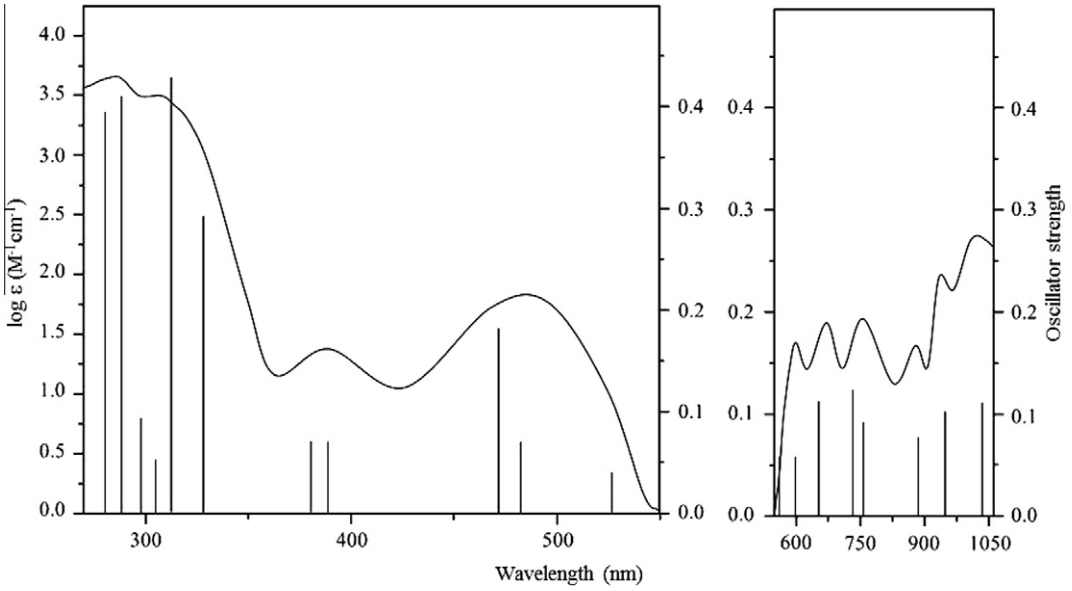

Fig. 7. The observed electronic spectrum in DMSO (curve) and the computed transitions resulting from ZINDO/S-CI calculations (lines) of complex **2**.

states is much larger than that in the quintet ($S = 2$) state and may be too large compared to the X-band quantum energy [44]. Therefore, the X-band spectra of both complexes can be attributed to the quintet ($S = 2$) spin state. The EPR data of the dimeric complexes **1** and **2** were analyzed using the following Hamiltonian:

$$\hat{H} = g\mu_B H \cdot \sum_{i=1}^{2} S_{iz} + D\sum_{i=1}^{2}(S_{iz}^2 - \frac{1}{3}S(S+1)) + E\sum_{i=1}^{2}(S_{iy}^2 - S_{ix}^2) - 2S_i\hat{J}S_j$$

where g is the Lande g-tensor, μ_B is the Bohr magneton, D is the single ion uniaxial anisotropy parameter corresponding to the easy axis of each chromium ion and E is a parameter corresponding to the transverse axes. $\hat{J}$ is a tensor describing the isotropic exchange, anisotropic exchange and dipolar coupling between the two chromium ions [41,45,46].

Based on the above-mentioned Hamiltonian, the quintet spectrum of complex **1** (Fig. 4) was simulated with the parameters $J = 23$ cm^{-1}, $g = 2.11$, $D = 0.074$ cm^{-1} and $E = 0.008$ cm^{-1}, assuming two similar chromium ions. The spectrum of complex **2** clearly indicates two slightly different chromium ions (Fig. 5). These are in good agreement with the structural data obtained by the parameterized PM3 semi-empirical calculations (Table 2). The experimental ESR spectrum of complex **2** was simulated with the parameters $J = 17$ cm^{-1}, $g_1 = 2.17$, $D_1 = 0.063$ cm^{-1} and $E_1 = 0.012$ cm^{-1} for site 1 and $g_2 = 2.055$, $D_2 = 0.065$ cm^{-1} and $E_2 = 0.0087$ cm^{-1} for site 2. Almost all the lines observed are seen in the simulated spectra, and in spite the crude model for line widths, the overall simulation of the experimental data are good. The calculated J values are comparable to the value reported for the di-μ-ethoxo bridged binuclear Cr(III) complex, $[Cr(Br\text{-}acac)_2OEt]_2$ [15]. The higher J value

Table 4
Energies, percent contribution from Cr, QX, bpy and EtO, and the main character of some frontier orbitals obtained from the ZINDO/S calculations for complexes **1** and **2**.

	Orbital[a]	Type[b]	Energy (eV)	%Cr_1	%Cr_2	%QX_1[c]	%QX_2	%bpy_1	%bpy_2	%EtO_1	%EtO_2	Main character
1	L+5	V	0.525	13.34	14.03	3.07	3.23	22.34	41.95	1.65	0.23	$Cr_1(d_{\sigma^*})$, $Cr_2(d_{\pi^*})$, $bpy_{1,2}(\pi^*)$
	L+4	V	0.492	0.90	21.05	1.74	6.05	7.37	60.72	0.83	1.29	$Cr_1(d_{\sigma^*})$, $Cr_2(d_{\pi^*})$, $bpy_2(\pi^*)$
	L+3	V	−0.070	12.67	15.70	4.05	3.73	28.72	28.28	3.26	3.55	$Cr_1(d_{\sigma^*})$, $Cr_2(d_{\pi^*})$, $bpy_{1,2}(\pi^*)$
	L+2	V	−0.418	37.08	11.81	2.26	1.20	41.83	13.91	0.85	0.93	$Cr_1(d_{\pi^*})$, $Cr_2(d_{\pi^*})$, $bpy_{1,2}(\pi^*)$
	L+1	V	−0.520	25.82	14.70	8.33	3.44	31.45	15.02	0.55	0.51	$Cr_1(d_{\pi^*})$, $Cr_2(d_{\sigma^*})$, $bpy_{1,2}(\pi^*)$
	L	V	−0.635	16.31	27.36	0.76	9.67	7.93	27.33	6.50	3.93	$Cr_1(d_{\sigma^*})$, $Cr_2(d_{\sigma^*})$, $bpy_2(\pi^*)$
	H	S	−3.659	23.70	11.81	17.39	1.32	26.65	13.55	3.26	2.19	$Cr_1(d_{\pi})$, $Cr_2(d_{\sigma})$, $QX_1(Op_{\pi})$, $bpy_1(\pi)$
	H−1	S	−3.777	14.81	20.64	11.10	10.24	10.42	28.52	2.17	1.96	$Cr_1(d_{\pi})$, $Cr_2(d_{\pi})$, $QX_1(Op_{\pi})$, $bpy_2(\pi)$
	H−2	O	−5.677	9.68	8.72	6.44	70.01	1.55	2.59	0.24	0.56	$Cr_1(d_{\pi})$, $Cr_2(d_{\pi})$, $QX_2(Op_{\pi})$
	H−3	O	−5.863	19.11	8.67	49.63	7.01	13.60	0.95	0.32	0.31	$Cr_1(d_{\pi})$, $Cr_2(d_{\pi})$, $QX_1(Op_{\pi})$, $bpy_1(\pi)$
	H−4	O	−6.942	39.71	22.54	20.09	6.46	5.33	1.01	3.87	3.12	$Cr_1(d_{\pi})$, $Cr_2(d_{\sigma})$, $QX_1(Op_{\pi})$
	H−5	O	−7.173	10.93	18.50	1.56	50.75	2.01	2.51	11.57	2.17	$Cr_1(d_{\pi})$, $Cr_2(d_{\pi})$, $QX_2(Op_{\pi})$, $EtO(Op_{\pi})$
2	L+5	V	0.669	26.76	3.71	3.28	2.30	33.47	29.49	0.48	0.33	$Cr_1(d_{\pi^*})$, $Cr_2(d_{\sigma^*})$, $bpy_{1,2}(\pi^*)$
	L+4	V	0.561	5.28	14.65	1.26	5.68	10.85	56.53	3.93	1.66	$Cr_1(d_{\sigma^*})$, $Cr_2(d_{\pi^*})$, $bpy_2(\pi^*)$
	L+3	V	0.050	18.31	20.72	4.05	6.73	11.61	29.22	5.38	3.22	$Cr_1(d_{\pi^*})$, $Cr_2(d_{\sigma^*})$, $bpy_2(\pi^*)$
	L+2	V	−0.103	19.43	17.09	6.58	7.22	24.46	21.77	1.74	1.41	$Cr_1(d_{\pi^*})$, $Cr_2(d_{\pi^*})$, $bpy_{1,2}(\pi^*)$
	L+1	V	−0.302	25.21	13.18	5.93	6.91	42.25	4.98	0.89	0.41	$Cr_1(d_{\pi^*})$, $Cr_2(d_{\sigma^*})$, $bpy_1(\pi^*)$
	L	V	−0.344	22.17	28.92	2.77	7.42	16.96	20.66	0.45	0.55	$Cr_1(d_{\sigma^*})$, $Cr_2(d_{\sigma^*})$, $bpy_{1,2}(\pi^*)$
	H	S	−3.496	16.25	14.86	12.57	9.62	23.56	19.94	1.11	1.95	$Cr_1(d_{\pi})$, $Cr_2(d_{\pi})$, $QX_{1,2}(Op_{\pi})$, $bpy_{1,2}(\pi)$
	H−1	S	−3.561	16.33	18.65	10.11	11.10	17.23	21.60	2.13	2.41	$Cr_1(d_{\pi})$, $Cr_2(d_{\pi})$, $QX_{1,2}(Op_{\pi})$, $bpy_{1,2}(\pi)$
	H−2	O	−5.493	7.42	6.88	35.25	42.54	2.48	2.10	1.15	1.87	$Cr_1(d_{\pi})$, $Cr_2(d_{\pi})$, $QX_{1,2}(Op_{\pi})$
	H−3	O	−5.597	10.39	8.90	33.72	31.28	9.57	4.47	0.76	0.74	$Cr_1(d_{\pi})$, (d_{π}), $Cr_2(d_{\sigma})$, $QX_1(Op_{\pi})$, $Q_{X2}(O_{\sigma})$
	H−4	O	−6.841	21.67	39.23	5.32	24.58	1.77	5.49	1.44	0.40	$Cr_1(d_{\pi})$, $Cr_2(d_{\pi})$, $QX_2(Op_{\pi})$
	H−5	O	−7.018	19.81	13.22	15.64	28.30	2.87	2.93	13.82	3.11	$Cr_1(d_{\pi})$, $Cr_2(d_{\sigma})$, $QX_1(Op_{\pi})$, $Q_{X2}(O_{\sigma})$ $EtO_1(Op_{\pi})$

[a] L and H represent the LUMO and HOMO, respectively. L+*n* indicates the *n*th molecular orbital above the LUMO and H−*n* indicates the *n*th molecular orbital below the HOMO.
[b] V, S and O represent unoccupied (virtual), singly occupied and doubly occupied molecular orbitals, respectively.
[c] QX is DCQX for complex **1**, and DMQX for complex **2**.

calculated for complex **1**, compared to that of complex **2**, could be attributed to the shorter Cr···Cr separation and the smaller Cr–O–Cr angle of the former complex [7,43].

The electronic absorption spectra of the dimeric complexes **1** and **2** recorded in DMSO solution at room temperature are represented in Figs. 6 and 7, respectively. Both spectra are comprised of three main features: (i) broad absorptions ($\log\varepsilon > 3.2\ M^{-1}\ cm^{-1}$) in the UV region (ii) two-weaker broad bands ($1 < \log\varepsilon < 2.0\ M^{-1}\ cm^{-1}$) in the visible region (iii) and multiple maxima ($\log\varepsilon \approx 0.2\ M^{-1}\ cm^{-1}$) in the 550–1050 nm region. The similarities of the absorption bands in the spectra of both complexes may suggest similar electronic structures for both complexes. However, the shifts in the position of the absorption band maxima may reflect the difference in energies of the orbitals from which these transitions originate in both complexes. The broad absorptions in the UV region can be assigned to ligand-to-metal charge-transfer transitions from the p_π orbitals of the quinoxalinediolate oxygen to the empty Cr(eg) and/or the half-filled Cr(t_{2g}) orbital [47], in addition to possible Cr(d_π) → bpy(π^*) metal-to-ligand charge-transfer transitions [48–50]. The weaker broad bands observed between 370 and 550 nm compares well with those reported for the spin-allowed d–d transitions of dinuclear chromium (III) complexes [2,51–53]. The very weak maxima observed in the spectra between 550 and 1050 nm are characteristic of dimeric complexes. Glerup et al. [52] have reported six weak maxima that were assigned to the spin-forbidden d–d transitions of the $[(Me_3\text{-tame})Cr(OH)_3Cr(Me_3\text{-tame})]^{3+}$ complex. These transitions are usually forbidden in monomeric Cr(III) complexes and become allowed in dimeric Cr(III) complexes as a result of antiferromagnetic coupling. Such special spectral features are most probably dependent on the magnitude of the antiferromagnetic exchange interactions since some dialkoxo-bridged complexes with *J* values lower than $10\ cm^{-1}$ did not show any intensity enhancements of these transitions [35]. These results may give further support for the *J* values calculated from the ESR data for the dimeric complexes **1** and **2**. The ZINDO/S-CI semi-empirical method was used to interpret the electronic transitions for the two dimeric complexes and the results give some insight on the orbitals responsible for these transitions.

The ZINDO/S method is parameterized to produce the UV–Vis electronic transitions and has been used to estimate the frontier molecular orbitals of the two dimeric complexes. This method has been previously used to reproduce the spectra of several complexes of the first row transition-metal series and more particularly for studying the spectroscopy of internal d–d excitations [54]. Also, it was successful in studying the electronic spectra of dinuclear Cr(III) and Co(III) complexes of bis(ditholene) [55].

Table 4 lists the results of ZINDO/S-CI energies, compositions and main character of some frontier molecular orbitals. At a first glance, it can be seen that the contributions of the bpy ligands are higher in the LUMOs, whereas the QX ligands have more contributions to the HOMOs. As a result, excitation of electrons from HOMOs to LUMOs would lead to Cr → bpy (MLCT) and/or QX → Cr (LMCT) depending on the %Cr in the HOMOs and LOMOs. The shape of the magnetic molecular orbitals (HOMO and LUMO) of the two dimeric complexes **1** and **2** are pictorially shown in Fig. 8. The highest occupied molecular orbital (HOMO) has a higher contribution from Cr(d_π), whereas the lowest unoccupied molecular orbital (LUMO) has Cr(d_{σ^*}) character. The energy gap ($\Delta E_{LUMO-HOMO}$) values of 3.02 and 3.15 eV for complexes **1** and **2**, respectively, may reflect the difference in the antiferromagnetic exchange interactions between the two Cr(III) centers in the two dimeric complexes.

The results of the calculated electronic transitions for the dimeric complexes **1** and **2** are shown in Figs. 6 and 7, respectively. The assignment of the computed electronic transitions is listed in Table 5. There are good agreements between the computed active transitions and the observed bands. As expected, the three broad absorptions observed in the UV region of the spectrum of complex **1** can be assigned to charge transfer transitions. The first band observed at 273 nm was assigned to the $EtO_1(Op_\pi) \rightarrow Cr_1(d_{\pi^*})$ ligand-to-metal charge-transfer transition with the major configuration

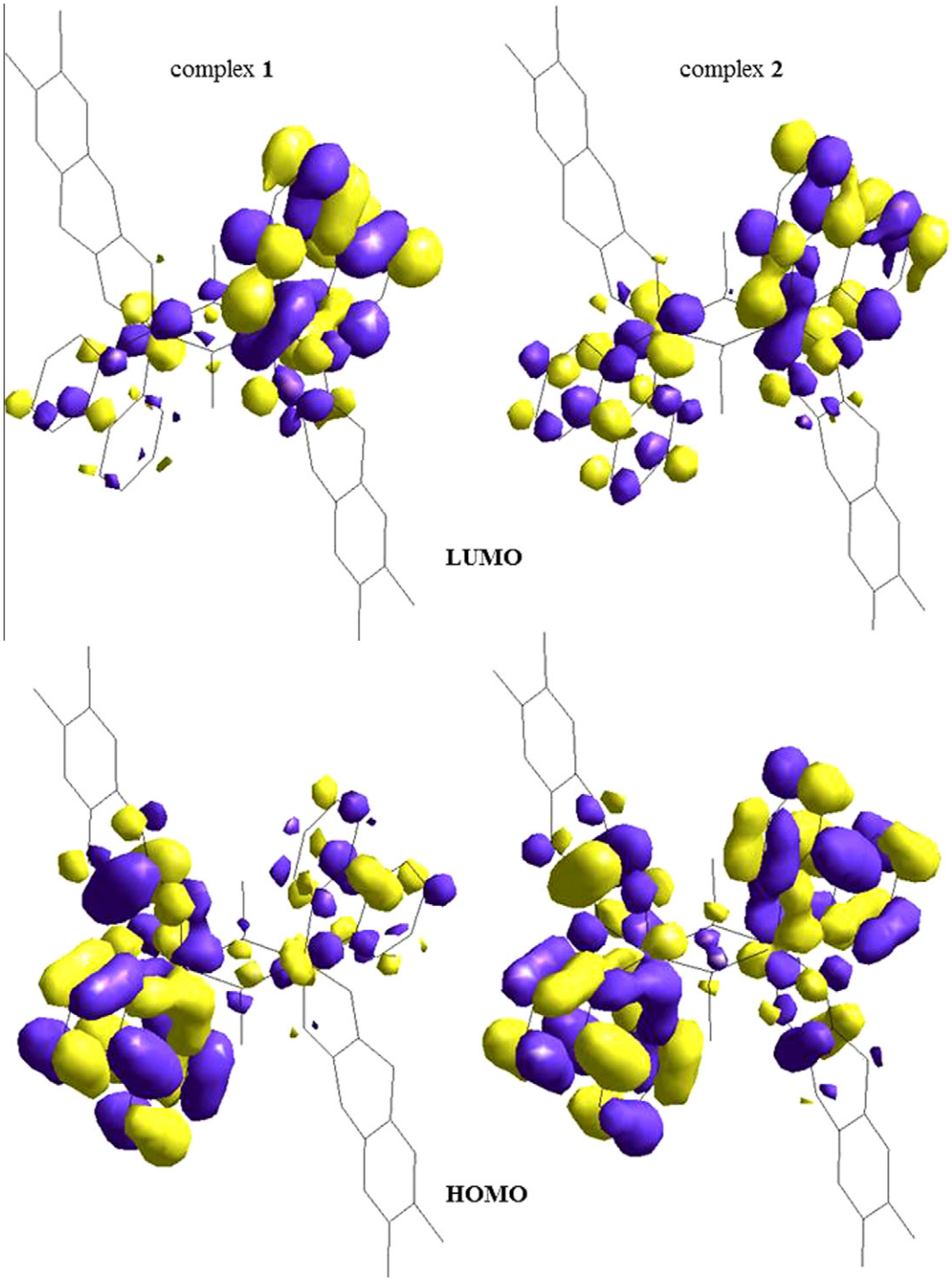

Fig. 8. The highest singly occupied (HOMO) and the lowest unoccupied (LUMO) molecular orbitals for complexes **1** and **2**.

0.67(H−5 → L+1). The second broad band observed at 287 nm, which was assigned to the $Cr(d_\pi) \rightarrow bpy(\pi^*)$ metal-to-ligand charge-transfer transition, was computed to have a contribution from four transitions with major configurations (H−1 → L+3), 0.99(H−1 → L+5), 0.72(H−4 → L+2) and 0.76(H−3 → L+3). The third band in the UV region, observed at 320 nm, was assigned to the $DCQX(Op_\pi) \rightarrow Cr(d_{\pi^*})$ ligand-to-metal charge-transfer transition and was computed to have a contribution from (H−1 → L+2), 0.67(H−2 → L+3), 0.73(H−3 → L+2) and 0.66(H−2 → L+5) transitions. For complex **2** only two broad bands were observed in the UV region of the spectrum, with the absence of the band corresponding to the $EtO(Op_\pi) \rightarrow Cr(d_{\pi^*})$ transition. A computed value of 267 nm for this transition, with the major contribution 0.65(H−5 → L+2), makes it difficult to be observed in the spectrum due to the solvent cut off. In contrast, to the absorption corresponding to the $Cr(d_\pi) \rightarrow bpy(\pi^*)$ transition of complex **1**, the observed band at 286 nm for complex **2** was computed to have a mixed contribution from $Cr_2(d_\pi) \rightarrow bpy_2(\pi^*)$ MLCT and QX_1-$O(p_\pi) \rightarrow Cr_1(d_{\pi^*})$ LMCT transitions (Table 5). A1though the UV spectrum of complex **2** showed a broad absorption band corresponding to a DMQX-O → Cr LMCT transition, similar to that of complex **1**, it was found that this absorption has a contribution

Table 5
Observed and calculated electronic absorption data for [Cr(DCQX)(bpy)EtO]$_2$ (**1**) and [Cr(DMQX)(bpy)EtO]$_2$ (**2**), and assignment of the electronic transitions.

	Observed		Calculated			Assignment
	λ^{obs} (nm)	log ε (M^{-1} cm^{-1})	λ^{calc} (nm)	Oscillator strength	Composition of transition	
1	1035	0.26	1045	0.111	0.62(H−2 → H−1)	$Cr_{1,2}(d_\pi) \rightarrow Cr_{1,2}(d_\pi)$ d–d
	933	0.22	942	0.106	0.65(H−2 → H)	$Cr_{1,2}(d_\pi) \rightarrow Cr_1(d_\pi)$ d–d/$Cr_{1,2}(d_\pi) \rightarrow Cr_2(d_\sigma)$ d–d
	851	0.16	849	0.062	0.70(H−3 → H−1)	$Cr_{1,2}(d_\pi) \rightarrow Cr_{1,2}(d_\pi)$ d–d
	757	0.18	779	0.101	0.72(H−3 → H)	$Cr_{1,2}(d_\pi) \rightarrow Cr_1(d_\pi)$ d–d/$Cr_{1,2}(d_\pi) \rightarrow Cr_2(d_\sigma)$ d–d
	644	0.17	660	0.135	0.59(H−4 → H−1)	$Cr_1(d_\pi) \rightarrow Cr_{1,2}(d_\pi)$ d–d
			642	0.063	0.59(H−4 → H)	$Cr_1(d_\pi) \rightarrow Cr_1(d_\pi)$ d–d/$Cr_1(d_\pi) \rightarrow Cr_2(d_\sigma)$ d–d
	609	0.15	591	0.068	0.62(H−5 → H−1)	$Cr_{1,2}(d_\pi) \rightarrow Cr_{1,2}(d_\pi)$ d–d
			556	0.100	0.64(H−5 → H)	$Cr_{1,2}(d_\pi) \rightarrow Cr_1(d_\pi)$ d–d/$Cr_{1,2}(d_\pi) \rightarrow Cr_2(d_\sigma)$ d–d
	476	1.86	512	0.056	0.46(H−3 → L)	$Cr_1(d_\pi) \rightarrow Cr_1(d_{\sigma^*})$ d–d
			474	0.099	0.87(H → L)	$Cr_1(d_\pi) \rightarrow Cr_1(d_{\sigma^*})$ d–d
			451	0.130	0.55(H−2 → L)	$Cr_1(d_\pi) \rightarrow Cr_1(d_{\sigma^*})$ d–d
	396	1.50	395	0.090	0.99(H−1 → L)	$Cr_1(d_\pi) \rightarrow Cr_1(d_{\sigma^*})$ d–d/$Cr_2(d_\pi) \rightarrow Cr_2(d_{\sigma^*})$ d–d
			372	0.118	(H → L+1)	$Cr_1(d_\pi) \rightarrow Cr_2(d_{\sigma^*})$ d–d
	340	3.21	344	0.336	0.69(H−2 → L+2)	$QX_2(Op_\pi) \rightarrow Cr_2(d_{\pi^*})$ LMCT
	320	3.68	327	0.448	(H−1 → L+2)	$QX_1(Op_\pi) \rightarrow Cr_1(d_{\pi^*})$ LMCT
			322	0.584	0.67(H−2 → L+3)	$QX_2(Op_\pi) \rightarrow Cr_2(d_{\pi^*})$ LMCT
			313	0.061	0.73(H−3 → L+2)	$QX_1(Op_\pi) \rightarrow Cr_1(d_{\pi^*})$ LMCT
			305	0.061	0.66(H−2 → L+5)	$QX_2(Op_\pi) \rightarrow Cr_2(d_{\pi^*})$ LMCT
	287	3.55	301	0.097	(H−1 → L+3)	$Cr_1(d_\pi) \rightarrow bpy_1(\pi^*)$ MLCT
			292	0.408	0.99(H−1 → L+5)	$Cr_2(d_\pi) \rightarrow bpy_2(\pi^*)$ MLCT
			285	0.088	0.72(H−4 → L+2)	$Cr_1(d_\pi) \rightarrow bpy_1(\pi^*)$ MLCT
			280	0.542	0.76(H−3 → L+3)	$Cr_1(d_\pi) \rightarrow bpy_1(\pi^*)$ MLCT
	273	3.63	274	0.370	0.67(H−5 → L+1)	$EtO_1(Op_\pi) \rightarrow Cr_1(d_{\pi^*})$ LMCT
2	1024	0.28	1034	0.111	0.62(H−2 → H−1)	$Cr_{1,2}(d_\pi) \rightarrow Cr_{1,2}(d_\pi)$ d–d
	942	0.24	948	0.102	0.65(H−2 → H)	$Cr_{1,2}(d_\pi) \rightarrow Cr_{1,2}(d_\pi)$ d–d
	882	0.11	884	0.077	0.69(H−3 → H−1)	$Cr_1(d_\pi) \rightarrow Cr_{1,2}(d_\pi)$ d–d
	754	0.19	758	0.092	0.78(H−3 → H)	$Cr_1(d_\pi) \rightarrow Cr_{1,2}(d_\pi)$ d–d
			732	0.123	0.52(H−4 → H−1)	$Cr_{1,2}(d_\pi) \rightarrow Cr_{1,2}(d_\pi)$ d–d
	671	0.19	653	0.112	0.57(H−4 → H)	$Cr_{1,2}(d_\pi) \rightarrow Cr_{1,2}(d_\pi)$ d–d
	600	0.17	598	0.058	0.60(H−5 → H−1)	$Cr_1(d_\pi) \rightarrow Cr_{1,2}(d_\pi)$ d–d
			560	0.058	0.63(H−5 → H)	$Cr_1(d_\pi) \rightarrow Cr_{1,2}(d_\pi)$ d–d
	485	1.84	528	0.040	0.57(H−1 → L+4)	$Cr_1(d_\pi) \rightarrow Cr_1(d_{\sigma^*})$ d–d
			483	0.071	0.81(H → L)	$Cr_1(d_\pi) \rightarrow Cr_1(d_{\sigma^*})$ d–d/$Cr_2(d_\pi) \rightarrow Cr_2(d_{\sigma^*})$ d–d
			472	0.182	0.74(H → L+3)	$Cr_2(d_\pi) \rightarrow Cr_2(d_{\sigma^*})$ d–d
	388	1.40	389	0.070	0.99(H−1 → L)	$Cr_1(d_\pi) \rightarrow Cr_1(d_{\sigma^*})$ d–d/$Cr_2(d_\pi) \rightarrow Cr_2(d_{\sigma^*})$ d–d
			381	0.071	(H−1 → L+1)	$Cr_2(d_\pi) \rightarrow Cr_2(d_{\sigma^*})$ d–d
	329	2.89	328	0.293	0.68(H−2 → L+3)	$QX_1(Op_\pi) \rightarrow Cr_1(d_{\pi^*})$ LMCT/$QX_2(Op_\pi) \rightarrow Cr_2(d_{\pi*})$ LMCT
	308	3.51	312	0.430	0.74(H−2 → L+2)	$QX_1(Op_\pi) \rightarrow Cr_1(d_{\pi^*})$ LMCT/$QX_2(Op_\pi) \rightarrow Cr_2(d_{\pi^*})$ LMCT
			305	0.053	0.71(H−3 → L+2)	$QX_1(Op_\pi) \rightarrow Cr_1(d_{\pi^*})$ LMCT
			298	0.094	0.70(H−3 → L+3)	$QX_1(Op_\pi) \rightarrow Cr_1(d_{\pi^*})$ LMCT/$QX_2(Op_\sigma) \rightarrow Cr_2(d_{\sigma^*})$ LMCT
	286	3.67	288	0.411	(H → L+5)	$Cr_2(d_\pi) \rightarrow bpy_2(\pi^*)$ MLCT/$QX_1(Op_\pi) \rightarrow Cr_1(d_{\pi^*})$ LMCT
			281	0.396	(H−1 → L+5)	$Cr_2(d_\pi) \rightarrow bpy_2(\pi^*)$ MLCT/$QX_1(Op_\pi) \rightarrow Cr_1(d_{\pi^*})$ LMCT
			267	0.327	0.65(H−5 → L+2)	$EtO_1(Op_\pi) \rightarrow Cr_1(d_{\pi^*})$ LMCT

from $DMQX_1(Op_\pi) \rightarrow Cr_1(d_{\pi^*})$ and $DMQX_2(Op_\pi) \rightarrow Cr_2(d_{\pi^*})$ in addition to the $DMQX_2(Op_\sigma) \rightarrow Cr_2(d_{\sigma^*})$ transition.

The ligand-field d–d transitions observed in the visible region were well predicted by ZINDO/S-CI calculations. Two broad absorption bands were observed at 476 and 396 nm for complex **1** and similar bands were observed at 485 and 388 nm for complex **2**. These two bands in each complex can be related to the spin-allowed d–d transitions in octahedral symmetry, $^4A_{2g} \rightarrow {}^4T_{2g}$ and $^4A_{2g} \rightarrow {}^4T_{1g}$, respectively. ZINDO/S calculations showed that the lower energy band has a contribution from the transitions 0.46(H−3 → L), 0.87(H → L), 0.55(H−2 → L) for complex **1** and 0.57(H−1 → L+4), 0.81(H → L), 0.74(H → L+3) for complex **2**. On the other hand, the higher energy band could be analyzed into two transitions with major configurations 0.99(H−1 → L), (H → L+1) for complex **1** and 0.99(H−1 → L), (H−1 → L+1) for complex **2**. Consistent with these assignments, Byun et al. [56] have performed an approximate deconvolution of the two bands observed for the d–d transition at 541 and 390 nm, followed by a least-square fitting procedure and obtained four peaks at 556, 535, 398 and 385 nm which were assigned to $^4E(^4T_{2g}$ in O_h symmetry), $^4B_2(^4T_{2g})$, $^4E(^4T_{1g})$ and $^4A_2(^4T_{1g})$, respectively. It is worth noting that the intensity enhancement observed for these transitions can be attributed to the contribution of QX and bpy ligands in the MOs involved in the d–d transitions (Table 4). This might add a small percentage of charge-transfer transitions to the expected ligand-field d–d transitions.

The most spectacle observation of the spectrum of the two dimeric complexes is very weak maxima observed in spectra between 550 and 1050 nm, which was predicted by the ZINDO/S calculation as transitions between doubly occupied MOs [(H−2)–(H−5)] and singly occupied MOs (H and H−1). These transitions should be present in the monomeric Cr(III) complexes since they possess doubly and singly occupied MOs too, but we believe that these transitions, which are characteristic of many dinuclear transition metal complexes, are of too low intensity (spin-forbidden) in the analogous monomeric complexes to be observed. Such enhancement in intensity observed for the dinuclear complexes **1** and **2** can be attributed to the involvement of the two Cr(III) centers in these transitions. Table 5 shows that these lower energy absorptions have contributions from doubly occupied MOs→ singly occupied MOs: $Cr_1(d_\pi) \rightarrow Cr_1(d_{\pi^*})$, $Cr_2(d_\pi) \rightarrow Cr_2(d_{\pi^*})$, $Cr_1(d_\pi) \rightarrow Cr_2(d_{\pi^*})$, $Cr_2(d_\pi) \rightarrow Cr_1(d_{\pi^*})$, $Cr_1(d_\pi) \rightarrow Cr_2(d_{\sigma^*})$ and $Cr_2(d_\pi) \rightarrow Cr_2(d_{\sigma^*})$ transitions.

The antibacterial activities of the quinoxaline-2,3-dione ligands (DCQX and DMQX) and their dichromium(III) complexes (**1** and **2**) were tested against the bacterial species *S. aureus* and *E. coli* by the

Table 6
The antimicrobial activities of the DCQX and DMQX ligands and their dichromium complexes.

Sample	log*P*[d]	Inhibition zone diameter (mm/mg sample)			
		Escherichia coli (Gram-negative)	*Staphylococcus aureus* (Gram-positive)	*Aspergillus flavus*	*Candida albicans*
DMSO[a]		0.0	0.0	0.0	0.0
Tetracycline[b]	+0.48	31	33	–	–
Amphotericin B[c]		–	–	17	21
DCQX	−2.54	15	16	12	12
DMQX	−1.78	21	19	0.0	14
Complex **1**	−2.40	18	16	16	17
Complex **2**	−0.89	22	20	14	15

[a] DMSO solvent was used as a negative control.
[b] Standard antibacterial agent.
[c] Standard antifungal agent.
[d] Lipophilicity (log*P*) values calculated using QSAR.

Kirby Bauer disc diffusion method. Also, the ligands and complexes were tested against the fungal species *A. flavus* and *C. albicans*, cultured on agar medium and also performed by the disc diffusion method. Tetracycline was used as the standard antibacterial agent whereas Amphotericin B was used in the technique as the standard antifungal agent. The results of the antimicrobial activity studies are presented in Table 6.

The inhibition zone diameter measured for the studied compounds against Gram negative bacteria (*E. coli*) and Gram positive bacteria (*S. aureus*) indicated that both complexes showed higher inhibitory activities compared to their free ligands. In addition, significant bacterial inhibition activities were observed for complex **2** and its free DMQX ligand compared to the analogous complex **1** and the free DCQX ligand.

Understanding the role of chemical structure on influencing biological activity is very important. Studies on the structure–activity relationship have shown the importance of the lipophilic nature of biologically active molecules [57,58]. The lipophilicity modifies the penetration of bioactive molecules through the non-polar cell of bacteria membranes. The computer program QSAR implemented in HYPERCHEM 7.5 predicts the lipophilicity values of chemical compounds (log*P*) using the atom-additive method [59]. The program lists the atom contributions of each atom type and calculates the log*P* value by summing up all the atom contributions. The calculated log*P* values listed in Table 6 are in good agreement with the bacterial inhibition activities observed for the studied compounds, with complex **2** and its free DMQX ligand having higher lipophilicity log*P* values after the standard tetracycline antibiotic. Lipophilicity of compounds usually increases with increasing methyl groups and aromatic rings in the compounds. This might explain the higher log*P* values of the DMQX ligand and its dichromium complex **2**. Also, the presence of coordinated bpy ligands in complex **2** may explain its higher lipophilicity compared to the free DCQX ligand.

The fugal activities of the studied complexes shown in Table 6 indicate that these compounds inhibit fungal growth by a different mechanism than that suggested for the inhibition of bacteria strains. While the DMQX ligand showed a high inhibitory activity against bacteria, it did not show any activity against *A. flavus* fungus. Also, complex **1** showed the highest inhibitory activities against both of the studied fungi. One of the antifungal mechanisms that may explain the higher inhibition activity of complex **1** is the binding of Cr metal to the chitin component of the fungal cell membrane after the cleavage of complex **1** to the monomeric [Cr(DCQX)(bpy)EtO] unit. Since chitin is a trace, a critical component of the fungal cell wall, and some inhibitors of chitin synthesis demonstrate antifungal activity. Effective binding of chromium to pure chitin has already been reported and it can be supposed that these fungal wall-polymers also play a role in the biosorption of chromium by the intact cell wall of the fungi [60]. In addition, Ebner et al. [61] have investigated the biosorption of chromium(III) by whole cells and isolated cell walls of fungi, and reported the fast initial sorption of Cr(III) on the cell wall was found, reaching 80% of the calculated maximum load after 30 min. contact time. However, the final biosorption maximum could be reached after 2 h. The suggested mechanism by cleavage of the bridging Cr–O bond has gained further support from the weaker bond calculated for complex **1**, with an average of 1.984 Å compared to the average bond length of 1.976 Å calculated for complex **2** (Table 2). Moreover, the charges calculated by the parameterized semi-empirical PM3 method on the two Cr centers were 0.384 and 0.386 for complex **1**, whereas the values of 0.329 and 0.338 were calculated for complex **2**. This gives further support for the ability of chromium ions in complex **1** to strongly bind to chitin.

References

[1] F. Tuczek, E.I. Solomon, Coord. Chem. Rev. 219–221 (2001) 1075.
[2] A.B.P. Lever, Inorganic Electronic Spectroscopy, second ed., Elsevier Science Publishers B.V., New York, 1984.
[3] R. Schenker, H. Weihe, H.U. Gudel, Inorg. Chem. 38 (1999) 5593.
[4] D.S. McClure, J. Chem. Phys. 39 (1963) 2850.
[5] H.J. Schugar, G.R. Rossman, J. Thibeault, H.B. Gray, Chem. Phys. Lett. 6 (1970) 26.
[6] N. Clement, C. Toussaint, G. Rogez, C. Loose, J. Kortus, L. Brelot, S. Choua, S. Dagorne, P. Turek, R. Welter, Dalton Trans. 39 (2010) 1.
[7] J. Glerup, D.J. Hodgson, E. Pedersen, Acta Chem. Scand., A 37 (1983) 161.
[8] A.S. Attia, B.J. Conklin, C.W. Lange, C.G. Pierpont, Inorg. Chem. 35 (1995) 1033.
[9] A.S. Attia, M.F. El-Shahat, Polyhedron 26 (2007) 791.
[10] M.Y. Nassar, A.S. Attia, S. Adawy, M.F. El-Shahat, J. Mol. Struct. 1026 (2012) 88.
[11] A.S. Attia, S.F. El-Mashtoly, M.F. El-Shahat, Polyhedron 22 (2003) 895.
[12] H. Thakuria, G. Das, J. Chem. Sci. 118 (2006) 425.
[13] W.A. Bauer, W.M. Kirby, C. Sherris, M. Turck, Am. J. Clin. Pathol. 45 (1966) 493.
[14] HYPERCHEM 7.5, Hypercube Inc., 2003.
[15] E.D. Estes, R.P. Scaringe, W.E. Hatfield, D.J. Hodgson, Inorg. Chem. 15 (1976) 1179.
[16] M.A. Ahmed, H. Fjellvag, A. Kjekshus, D.S. Wragg, N.S. Gupta, Z. Anorg. Allg. Chem. 637 (2011) 56.
[17] K.N. Raymond, S.S. Isied, L.D. Brown, F.R. fronczek, J.H. Nibert, J. Am. Chem. Soc. 98 (1976) 1767.
[18] J.T. Veal, W.H. Hatfield, D.J. Hodgson, Acta Crystallogr., Sect. B 29 (1973) 12.
[19] N.F. Brennan, B. Blom, S. Lotz, P.H. van Rooyen, M. Landman, D.C. Liles, M.J. Green, Inorg. Chem. Acta 361 (2008) 3042.
[20] M. Mohr, J.P. McNamara, H. Wang, S.A. Rajeev, J. Ge, C.A. Morgado, I.H. Hillier, Faraday Discuss. 124 (2003) 413.
[21] J.J.P. Stewart, J. Mol. Model 13 (2007) 1173.
[22] A.P. Scott, L. Radom, J. Phys. Chem. 100 (1996) 16502.
[23] A.D. Bacon, M.C. Zerner, Theor. Chim. Acta 32 (1973) 111.
[24] M. Kotzian, N. Roesch, M.C. Zerner, Theor. Chim. Acta 81 (1992) 201.
[25] K.K. Stavrev, M.C. Zerner, T.J. Meyer, J. Am. Chem. Soc. 117 (1995) 8684.
[26] K.K. Stavrev, M.C. Zerner, J. Chem. Phys. 102 (1995) 34.
[27] S. Stoll, A. Schweiger, J. Magn. Reson. 178 (2006) 42.
[28] C.G. Pierpont, R.M. Buchanan, Coord. Chem. Rev. 38 (1981) 45.
[29] A.S. Attia, C.G. Pierpont, Inorg. Chem. 37 (1998) 3051.
[30] A.S. Attia, S. Bhattacharya, C.G. Pierpont, Inorg. Chem. 34 (1995) 4427.
[31] K. Kovacs, A.A. Kamnev, J. Mink, C. Nemeth, E. Kuzmann, T. Megyes, T. Grosz, H.M. Schweiger, A. Vertes, Struct. Chem. 17 (2006) 105.
[32] P.A. Wicklund, D.G. Brown, Inorg. Chem. 15 (1976) 396.

[33] D.G. Brown, W.L. Johnson, Z. Naturforsch. 34B (1979) 712.
[34] A.S. Attia, Polyhedron 26 (2007) 2550.
[35] C.S. Wu, G.R. Rossman, H.B. Gray, G.S. Hammond, H.J. Schugar, Inorg. Chem. 11 (1972) 990.
[36] M.W. Lynch, M. Valentine, D.N. Hendrickson, J. Am. Chem. Soc. 104 (1982) 6982.
[37] J.S. Strukl, J.L. Walter, Spectrochem. Acta A 27 (1971) 223.
[38] A.S. Attia, Spectrochem. Acta A 67 (2007) 1339.
[39] A.G. Brolo, Z. Jiang, D.E. Irish, J. Electroanal. Chem. 547 (2003) 163.
[40] D.J. Darensbourg, E.B. Frantz, J.R. Andreatta, Inorg. Chem. Acta 360 (2007) 523.
[41] J. Glerup, P.A. Goodson, D.J. Hodgson, M.A. Masood, K. Michelsen, Inorg. Chem. Acta 358 (2005) 295.
[42] K. Michelsen, E. Pedersen, Acta Chem. Scand., A 37 (1983) 141.
[43] D. Kang, Bull. Korean Chem. Soc. 29 (2008) 963.
[44] V.V. Semenaka, O.V. Nesterova, V.N. Kokozay, V.V. Dyakonenko, R.I. Zubatyuk, O.V. Shishkin, R. Boca, J. Jezierska, A. Ozarowski, Inorg. Chem. 49 (2010) 5460.
[45] D. Burdinski, E. Bill, F. Birkelbach, K. Wieghardt, P. Chaudhuri, Inorg. Chem. 40 (2001) 1160.
[46] B. Cage, J.H. McNeely, K. Davis, A.J. Mihovilovich, B. Gopalakrishnan, B. Haferkamp, T. Rajh, B.D. Santarsiero, Polyhedron 29 (2010) 3021.
[47] R.K. Dean, S.L. Granville, L.N. Dawe, A. Decken, K.M. Hattenhauer, C.M. Kozak, Dalton Trans. 39 (2010) 548.
[48] H. Chang, K. Mochizuki, S. Kitagawa, Inorg. Chem. 41 (2002) 4444.
[49] D.M. Adams, L. Noodleman, D.N. Hendrickson, Inorg. Chem. 36 (1997) 3966.
[50] A.B.P. Lever, P.R. Auburn, E.S. Dodsworth, M. Haga, W. Liu, M. Melnik, W.A. Nevin, J. Am. Chem. Soc. 110 (1988) 8076.
[51] J. Glerup, S. Larsen, H. Weihe, Acta Chem. Scand. 45 (1991) 444.
[52] J. Glerup, S. Larsen, H. Weihe, Acta Chem. Scand. 47 (1993) 1154.
[53] L. Zhang, Y. Wang, W. Gu, X. Liu, D. Liao, Inorg. Chem. Commun. 9 (2006) 46.
[54] W.P. Anderson, W.D. Edwards, M.C. Zerner, Inorg. Chem. 25 (1986) 2728.
[55] A. Bencini, C.A. Daul, A. Dei, F. Mariotti, H. Lee, D.A. Shultz, L. Sorace, Inorg. Chem. 40 (2001) 1582.
[56] J.C. Byun, Y.C. Park, J.S. Youn, C.H. Han, N.H. Lee, Bull. Korean Chem. Soc. 26 (2005) 634.
[57] H. Ertepinarl, Y. Gok, O. Geban, S. Ozden, Eur. J. Med. Chem. 30 (1995) 171.
[58] A. Khalafi-Nezhad, M.N. Soltani Rad, H. Mohalbatkar, Z. Asrari, B. Hemmateenejad, Bioorg. Med. Chem. 13 (2005) 1931.
[59] A.K. Ghose, A. Pritchet, G.M. Crippen, J. Comput. Chem. 9 (1988) 80.
[60] V.W.D. Chui, K.W. Mok, C.Y. Ng, B.P. Luong, K.K. Ma, Environ. Int. 22 (1996) 463.
[61] C. Ebner, T. Pümpel, M. Gamper, Eur. J. Min. Process. Environ. Protect. 2 (2002) 168.